

# Supporting Information

## X-ray crystallographic and computational studies of the O<sub>2</sub>-tolerant [NiFe]-hydrogenase 1 from *Escherichia coli*.

Anne Volbeda, Patricia Amara, Claudine Darnault, Jean-Marie Mouesca, Alison Parkin, Maxie M. Roessler, Fraser A. Armstrong and Juan C. Fontecilla-Camps\*

### Material and Methods

#### 1. Protein expression and purification.

The *E. coli* K-12 strain used in this study was FTH004 (1). As previously described (1), it carries an engineered *hyaABCDEF* operon encoding a modified HyaA protein bearing a RSH<sub>6</sub> affinity tag at its extreme C terminus. FTH004 produces His-tagged *EcHyd-1* at wild-type levels under native regulatory and biosynthetic control.

The enzyme purification protocol was based on the previously published methodology (2). The bacteria were cultured anaerobically at 37 °C in LB medium supplemented with 0.5 % (w/v) glycerol and 0.4 % (w/v) sodium fumarate. The starter cultures (0.1 %) were grown aerobically at 37 °C in LB medium. To isolate *EcHyd-1*, cells were harvested during the stationary phase (centrifugation at 3,500 *g* for 12 min at 4 °C). The pelleted cells were re-suspended by shaking at 200 rpm at 25 °C for 30 min in 100 mM Tris, pH 7.5, 1 mM EDTA, 50 mM NaCl, supplemented with 10 g mL<sup>-1</sup> of DNase I and 50 g mL<sup>-1</sup> of lysozyme (both from Sigma), and Complete EDTA-free protease inhibitor mixture tablets (Roche Molecular Biochemicals) at the manufacturer's recommended concentration.

All further purification stages were conducted at 4 °C or on ice. The cells were disrupted by three passages through a French pressure cell at 20 kPSI. Any un-lysed cells were removed by centrifugation at 3,500 *x g* for 30 min. Membrane fractions were then prepared from the supernatant by ultracentrifugation at 150,000 *x g* for 1 h. The pelleted membrane fraction was re-suspended in 100 mM Tris, pH 7.5, 350 mM NaCl, and the suspension adjusted to a protein concentration of approximately 10 mg mL<sup>-1</sup>. Protease inhibitor tablets were again added at the appropriate concentration. The detergent Triton X-100 was added to the suspension to a final concentration of 3% w/v, and the membranes were solubilized by gentle stirring at 4 °C for 40 min. Insoluble material was removed by ultracentrifugation at 150,000 *x g* for 1 h. Dithiothreitol (DTT) and imidazole were added to the cleared supernatant (giving 1 and 40 mM, respectively), and the solution was applied to a Ni<sup>2+</sup>-loaded 5-mL HisTrap Chelating HP column (Amersham Biosciences) equilibrated in 20 mM Tris, pH 7.5, 350 mM NaCl, 60 mM imidazole, 1 mM DTT, 0.02% Triton X-100 (buffer A). The column was washed with 120 mL of buffer A and then developed in 55 mL of the same buffer using a linear gradient of imidazole to a final concentration of 750 mM. Fractions containing purified *EcHyd-1* as judged by absorbance at 420 and 280 nm were pooled and concentrated using a Vivaspinn 30KD cutoff filter. The imidazole concentration was then decreased by about 1:50 through dilution with an imidazole-free version of buffer A, followed by re-concentration.

#### 2. *EcHyd-1* Crystallization.

Attempts to crystallize the above sample were unsuccessful. Considering that the problem could be due to the nature of the detergent, we decided to replace Triton X-100 with n-dodecyl β-D-maltoside (DDM). The detergent exchange of the sample by dialysis was carried out overnight in a glove box against 5 L of a buffer containing 20mM Tris HCl pH 7.2, 150 mM NaCl, 1 mM DTT and 0.02% DDM (buffer B). This procedure was repeated again the next morning. The sample was then run through a Gel Filtration Superdex200 16/60 column (GE Healthcare) with buffer B. The eluted protein solution was applied to a hydroxyapatite column (Bio Gel HT Biorad) in a buffer containing 10 mM K<sub>2</sub>HPO<sub>4</sub>/KH<sub>2</sub>PO<sub>4</sub> pH 7.2, 150 mM NaCl, 1 mM DTT and 0.02% DDM; it was subsequently eluted with a gradient between 0 and 500 mM K<sub>2</sub>HPO<sub>4</sub>/KH<sub>2</sub>PO<sub>4</sub> pH 7.2, 150 mM NaCl, 1 mM DTT and 0.02% DDM, using 10 column volumes. *EcHyd-1* was collected at approximately 110 mM

$K_2HPO_4/KH_2PO_4$ . The sample to be used for the crystallization experiments was concentrated and buffer-exchanged using a Vivaspin 10 kDa cutoff filter and buffer B. A Rose Bengal test showed that the resulting *EcHyd-1* solution was concentrated to 5 mg/ml. The first as-isolated *EcHyd-1* crystals were obtained inside a dedicated glove box using a Gryphon robot (ArtRobbins) and one of the Hampton Crystal Screen conditions: 30% PEG4000, 200 mM  $LiSO_4$ , 100 mM Tris HCl pH 8.5, 150 mM NaCl, 1 mM DTT and 0.02% DDM. Rods of about 300 to 500  $\mu m$  in length were flash-cooled inside the glove box, after adding 20% glycerol, using the procedure of Vernède and Fontecilla-Camps (3).

In further experiments, *EcHyd-1* crystals were soaked in solutions containing 10 mM potassium ferricyanide and an additional redox mediator: 4-OH-1,4-naphthoquinone (OH-NQ). Because of its limited solubility, this compound was initially dissolved to a 20 mM concentration in DMSO and diluted to a final concentration of 2 mM in the soaking solutions. The crystals were soaked under air during 30 to 45 min in artificial mother liquor with 2% of added precipitant and without DTT. They were then transferred to a cryo-protectant solution containing an additional 20% glycerol and flash-cooled in liquid propane. Crystals soaked in the ferricyanide/OH-NQ solution were originally grown from the following crystallization conditions: 25% PEG 3350, 200 mM  $LiSO_4$ , 100mM Bis-Tris pH 5.5, 150 mM NaCl, 1 mM DTT and 0.02% DDM.

***H<sub>2</sub>-treated crystals.*** *EcHyd-1* crystals, grown in 21% PEG 3350, 200 mM  $LiSO_4$ , 100 mM HEPES pH 7.5, 150 mM NaCl, 1 mM DTT and 0.02% DDM, were soaked in the glove box for a few minutes in artificial mother liquor with 2% added precipitant and 1mM DTT. Subsequently, they were transferred to the same solution with added 20% glycerol, mounted in cryo-loops and exposed to approximately 8 bars of pure hydrogen gas in a small pressure cell during 10 min. They were then rapidly flash-cooled in liquid propane inside the glove box (3).

### 3. X-ray data collection and structure determination.

All X-ray data were collected at the European Synchrotron Radiation Facility (ESRF) in Grenoble (Table S1) keeping the crystals at  $\approx 100K$  under a cold nitrogen stream. The diffraction data were indexed, integrated and scaled with the XDS package (4), including a zero-dose correction in the scaling step (5). Most of the crystals used were orthorhombic (space group  $P2_12_12_1$ ) with cell dimensions  $a=93.7 \text{ \AA}$ ,  $b=97.4 \text{ \AA}$  and  $c=183.7 \text{ \AA}$ , and contained two hydrogenase heterodimers per asymmetric unit. The molecular replacement solution of the structure of the as-isolated enzyme using the program Phaser (6-8), and *Desulfovibrio fructosovorans* (*Df*) [NiFe]-hydrogenase (pdb deposition 1YQW) as a starting model, showed that the two heterodimers are related by almost perfect two-fold non-crystallographic symmetry (ncs). Both  $2mF_{obs}-\Delta F_{calc}$  and  $mF_{obs}-F_{calc}$  electron density maps (9) were used for manual model corrections with the program Coot (10). The signal-to-noise ratio of the internal protein regions in these maps was improved by two-fold averaging, using the in-house program Supermap. All the structures were refined, using slightly different strategies, with the program Refmac (11). The refined 1.67  $\text{\AA}$  resolution structure of the as-isolated enzyme was used as a starting model for both the oxidized and reduced forms. The 2.0  $\text{\AA}$  resolution ferricyanide/OH-NQ-oxidized structure was subsequently refined with tight ncs restraints for 92% of all protein atoms (the excluded 8% being involved in crystal packing or located in the most solvent-exposed regions). In the case of the  $H_2$ -reduced 1.47  $\text{\AA}$  resolution and the as-isolated 1.67  $\text{\AA}$  resolution structures ncs restraints were only used for the metal sites and their protein ligands, and only at the initial refinement stages. No metal-ligand restraints were used for the active site and the proximal cluster, which, because of its unprecedented structure, was refined with four freely moving irons and three freely moving sulfurs. In all the structures, anisotropic movements of the large subunits and the N-terminal and C-terminal domains of the small subunits were modeled with TLS refinement (12), using isotropic temperature factors for all atoms. In the final refinement cycles of the as-isolated and  $H_2$ -reduced structures, individual atomic anisotropic temperature factors were used instead. Refinement statistics are included in Table S1. The most significant structural differences between the as-isolated and  $H_2$ -reduced crystals were localized using two-fold averaged  $\Delta F_{obs}$ -maps, calculated with figure-of-merit-weighted model phases, after scaling of the structure factor amplitudes with the program Scaleit from the CCP4 package (13). The corresponding scaling statistics are included in Table S1. In such a  $\Delta F_{obs}$  map, positive and negative peaks correspond to atoms that either have shifted positions between the two structures or are missing in one of them. Figures 1, 2, 5, S1, S2 and S6 were prepared with the programs Molscript (14) and Raster3D (15) in addition to Conscript (16) to display electron density and cavity maps.

**Table S1.** X-ray data collection and refinement statistics.

<b>crystal</b>	as-isolated	oxidized	H <sub>2</sub> -reduced
<b>data:</b>			
pH	8.3	5.8	7.3
beamline	ID23-1	ID23-2	ID23-1
detector	ADSC	CCD	ADSC
$\lambda$ (Å)	0.94645	0.8726	1.00407
Total exposure (seconds)	129	120	130
transmission (%)	50	100	20
N <sub>hkl</sub>	194962	101239	283897
d <sub>max</sub> (Å)	1.67	2.0	1.47
R <sub>sym</sub> (%)	6.2	11.1	6.9
$\langle I/\sigma_I \rangle$	8.4	12.1	10.4
completeness (%)	99.8	87.6	99.8
B <sub>Wilson</sub> (Å <sup>2</sup> )	18.8	17.7	16.9
R <sub>scale</sub> (%)	0.0	13.3	18.0
<b>refinement:</b>			
resolution (Å)	30-1.67	25-2.0	25-1.47
R <sub>model</sub> (%)	12.0	14.1	12.2
R <sub>free</sub> (%)	16.8	17.7	16.0
atoms	15183	14932	15535
$\sigma_{\text{bond}}$ (Å)	0.011	0.013	0.010
$\sigma_{\text{angle}}$ (°)	1.24	1.26	1.22
$\langle B \rangle$ (Å <sup>2</sup> )	13.1	11.3	12.8

#### 4. Computational Studies.

All calculations on enzyme models were performed using programs from the Schrödinger Suite (17). The as-isolated *EcHyd-1* crystal structure was our starting model. To construct models for the proximal cluster in its most oxidized forms, (collectively referred to as PC3), we retained the proximal cluster conformation corresponding to the major oxidized form, which has the Fe<sub>4</sub> bound to both the amide nitrogen of Cys20 and the carboxylate O $\epsilon$  atom of Glu76. PC2 models (one-electron more reduced than PC3) were built with the other proximal cluster conformation with a deprotonated Glu76 distant from the cluster (see crystallographic results) and hydrogen bonded to Trp11 (named PC2<sup>-</sup>). This arrangement is also found in the O<sub>2</sub>-sensitive *Df* hydrogenase (18). Hydrogen atoms were added to the models and the protonation state of Asp, Glu and His residues were optimized with suitable water molecule orientations. We focused our attention on the putative proton transfer pathway from the proximal cluster to the active site that we have described earlier (19). The different protonations and/or hydrogen orientations in Glu16, His13, Thr18, Glu28<sub>L</sub> and Cys576<sub>L</sub> (L denotes large subunit residues), were investigated in order to reproduce their main conformations in the as-isolated model (see below).

Hybrid quantum mechanical (QM) / molecular mechanical (MM) potentials in the QSite program (17) allowed us to describe accurately the conformation of the proximal cluster and the residues in its vicinity, while taking into account the effect of the protein matrix. The quantum part consisted of i) the four Fe ions and the three inorganic sulfurs; ii) atoms from C $\alpha$  of Cys17 to C $\alpha$  of Thr21 (including Cys17, Cys19 and Cys20, which coordinate the proximal cluster) as well as the C $\beta$  and S $\gamma$  atoms of Cys115, Cys120, Cys149 and the C $\delta$ , N $\epsilon$ , C $\zeta$ , and N $\eta$  atoms of Arg74<sub>L</sub> which interact with the proximal cluster; iii) the carboxylate groups of Glu28<sub>L</sub>, Glu16 and Glu76 and iv) His13 and Trp11 side chains. The LACVP\*\* basis set (20, 21) was used for metals, whereas the 6-31G\*\* basis set was applied to all other atoms treated quantum mechanically. Density Functional Theory (DFT) was used for the QM part while the OPLS-2005 force field (22) was employed for the rest of the enzyme. Link atoms (23) were placed at the QM (C $\beta$ ) / MM (C $\alpha$ ) junction of Cys115, Cys120 and Cys149, the QM (C $\alpha$ ) / MM (N) junction of Cys17, the QM (N) / MM (C $\alpha$ ) junction of Thr21, the QM (C $\delta$ ) / MM (C $\gamma$ ) junction of Glu16, Arg74 and Glu76 and at the QM (C $\gamma$ ) / MM (C $\beta$ ) junction of His13 and Trp11. This resulted in 106 QM atoms. To characterize the

PC3 state, models with deprotonated and protonated (on the distal oxygen relative to Fe<sub>4</sub>) Glu76 were constructed whereas the amide of Cys20 was kept deprotonated because its nitrogen atom is clearly bound to Fe<sub>4</sub> in the X-ray structure (see Results section). The total charge of the PC3 structure, based on the [4Fe-3S] fragment, the six cysteine residues and the amido N that coordinate it is -2 or -3, depending on whether a bound Glu76 is protonated or not. These models are called PC3<sup>H</sup> and PC3<sup>-</sup>, respectively. An additional model called PC3<sub>d</sub><sup>-</sup> was constructed with a deprotonated Glu76 in the distal position it adopts in the PC2 state (Table 1).

Assuming that our X-ray models have the electronic configurations found by EPR and Mössbauer spectroscopic studies, we constructed a proximal cluster with total spins of S=0 and S=1/2 (24, 25) for the PC2 and PC3 models, respectively. We model the pure spin S=1/2 state, which cannot be obtained by standard DFT methods, by building corresponding Ms=1/2 broken symmetry (BS) states. These are, however, not pure spin states but states of mixed spin and spatial symmetry, which can be considered to be, as a first approximation, a superposition of four spin uncoupled iron monomers whose local high spin orientations  $\alpha$  or  $\beta$  are controlled during a DFT calculation. In the case of PC3, which has three ferric and one ferrous ions, six different BS states can be envisioned, labeled according to where the mixed-valence pair is located: BS12 means that iron sites 1 and 2 bear the mixed-valence pair, and iron sites 3 and 4 the ferric pair. Computationally, and starting from the cluster high-spin S=19/2 state, we flipped two of the four iron spins that generated the six initial BS states, namely, using the numbering of Fig. 3, BS13 (-4/2,+5/2,-5/2,+5/2), BS24 (+5/2,-5/2,+5/2,-4/2), BS34 (+5/2,+5/2,-5/2,-4/2), BS23 (+5/2,-4/2,-5/2,+5/2), BS12 (-4/2,-5/2,+5/2,+5/2), BS14 (-5/2,+5/2,+5/2,-4/2) which were then converged. During electronic convergence, within a given parallel spin mixed-valence pair of Fe atoms, nothing constrains the extra electron to be localized or delocalized. Although in BS34 and BS12 the Fe<sub>3</sub> and Fe<sub>4</sub> are not magnetically coupled, they will be considered as a pair in all broken symmetry states (Fig. 3).

We originally used the B3LYP functional with 20% Hartree-Fock to optimize the geometry of our models. However, some Fe-S distances that were standard in the PC3 X-ray structural model at 2.3 Å were optimized at longer values. Consequently, we decided, following the recommendation of Szilagyi and Winslow (26) with respect to an optimal description of the covalency within iron sulfur clusters, to use a customized functional with 5% Hartree-Fock exchange.

For our first model, we tested different protonation states and/or hydrogen orientations for residues Glu16, His13, Thr18 and Glu28<sub>L</sub>. The arrangement closest to the major conformation observed in the as-isolated X-ray structural model for these residues had protonated Glu16 and Glu28<sub>L</sub> and doubly protonated His13; the proton of Glu28<sub>L</sub> was orientated towards the thiolate of the Cys576<sub>L</sub> ligand of the Ni ion at the active site whereas the Thr18 proton pointed towards Glu28<sub>L</sub>, and the proton from Glu16 was oriented towards Thr18. Interestingly, a deprotonated Glu16 and a protonated Glu76, or the opposite, are found to form hydrogen bonds.

The six BS electronic configurations described above for PC3<sup>H</sup> and PC3<sup>-</sup> were geometry-optimized on the QM/MM potential surface using this functional, which is consistent with the one we later used for our Mössbauer parameter calculations (see below). Atoms located beyond 14 Å from the [4Fe-3S] fragment were held fixed during minimizations.

The same procedure was employed to model the possible electronic configurations of putative PC2 models (reminder: one electron more reduced than PC3 models). Due to the presence of two mixed-valence pairs we had to construct only three models: BS12 ( $\equiv$  BS34) (+4/2,+5/2,-5/2,-4/2), BS13 ( $\equiv$  BS24) (-4/2,+5/2,-5/2,+4/2) and BS14 ( $\equiv$  BS23) (-5/2,+5/2,+4/2,-4/2). The total charge of the cluster is -2, including the [4Fe3S] part and the six cysteine residues that coordinate it.

To calculate the Mössbauer parameters using our PC3 models, we extracted the proximal cluster, the coordinating Cys17, Cys115, Cys120 and Cys149, the Cys19-Cys20 fragment and Glu76. Thus, each QM model comprised a [4Fe-3S] core (charge: +5) linked to 4 dangling cysteinyl groups (SCH<sub>2</sub>CH<sub>3</sub>, charge: -4) and to one tridentate S(CH<sub>2</sub>)<sub>2</sub>-N-(C=O)-(CH<sub>2</sub>)<sub>2</sub>S group (charge: -3). Such QM models, including the deprotonated amide nitrogen and either a protonated or deprotonated glutamate-like group CH<sub>3</sub>(C=O)(O<sup>-</sup> or OH), had a total charge of -3 or -2, respectively (see also Table 1). Three cases were considered: (i) PC3<sup>H</sup>, (ii) PC3<sup>-</sup> and (iii) no Glu76 (equivalent to a distal Glu76, PC3<sub>d</sub><sup>-</sup>).

In order to compare calculated Mössbauer quadrupole tensors with the available experimental data measured for the PC3 redox state (24), we performed additional DFT calculations on these models, using the Slater-based ADF2009 code (27) with triple- $\zeta$  basis sets for all atoms. We relied on the modified B3LYP exchange-correlation potential combining the VWN5 local functional (Vosko, Wilk, and Nusair: VWN LDA functional) (28) with 5% of Hartree-Fock exchange, as used for our previous QM/MM calculations.

For the quadrupole tensor [Q], we relied on an in-house program coupled to ADF output files, based on an analytical expression published elsewhere (29, 30) which we already successfully used in a previous work (31).

From the three eigenvalues of  $[Q]$ , we get  $\Delta E_Q = (Q_{ii})_{\max}(1+\eta^2/3)$  where  $\eta$  is the asymmetry parameter defined as  $\eta = |((Q_{ii})_{\text{int}} - (Q_{ii})_{\text{min}}) / (Q_{ii})_{\text{max}}|$ .

For the computation of g-tensors, we used an in-house program coupled to ADF output files, based on second order expressions of the local iron atoms' g-tensors:  $g(\text{Fe})_{ij} \approx (g_e + \Delta g_{\text{iso}}) \delta_{ij} - (\xi_{\text{Fe}} / S_{\text{Fe}}) (\Sigma_{\text{maj}} - \Sigma_{\text{min}}) \Sigma_n [ \langle o | L_i | n \rangle \langle n | L_j | o \rangle / (E_n - E_o) ]$  where  $\xi_{\text{Fe}}$  is the iron one-electron spin-orbit constant ( $400 \text{ cm}^{-1}$  for  $\text{Fe}^{2+}$  of local spin  $S_{\text{Fe}} = 2$ , and  $460 \text{ cm}^{-1}$  for  $\text{Fe}^{3+}$  of local spin  $S_{\text{Fe}} = 5/2$ ).  $g_e$  is the free-electron gyromagnetic ratio (of value 2.0023). The indices "maj" and "min" refer to majority and minority spin molecular orbitals (MOs), respectively (here, the MOs are mainly iron-containing and result in metal-to-metal contributions to the g-tensor).  $E_o$  and  $E_n$  are the energies of the ground and excited states, respectively.  $\Delta g_{\text{iso}}$  is an unknown shift constant (i.e. not directly computed) reflecting an average of all minor ligand-to-metal contributions.  $\Delta g_{\text{iso}}$  is usually in the range 0.01-0.03, depending on the iron ion redox state. All further details pertaining to the g-tensor computation methodology have been given elsewhere (32).

## Results

### 1. Crystallographic characterizations of metal sites.

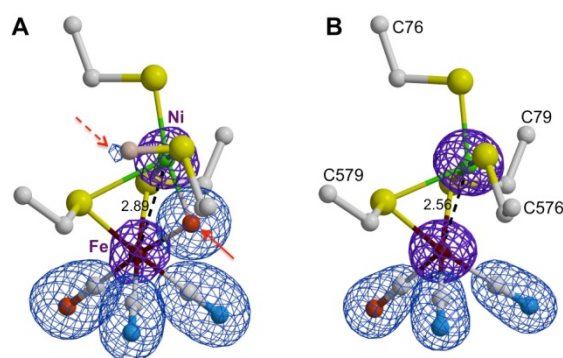


**Figure S1.** Comparison of the [NiFe] active site in **A**, as-isolated and **B**,  $\text{H}_2$ -reduced enzyme. The violet and blue grids depict averaged anomalous difference and omit electron density maps, respectively. The red arrows indicate sites which could have reacted with  $\text{O}_2$ , leading to a fully occupied putative bridging (hydr)oxide (solid line) and a putative minor sulfenic acid fraction (dashed line) in the as-isolated enzyme. The Ni-Fe distance in the two structures is indicated in Å units.

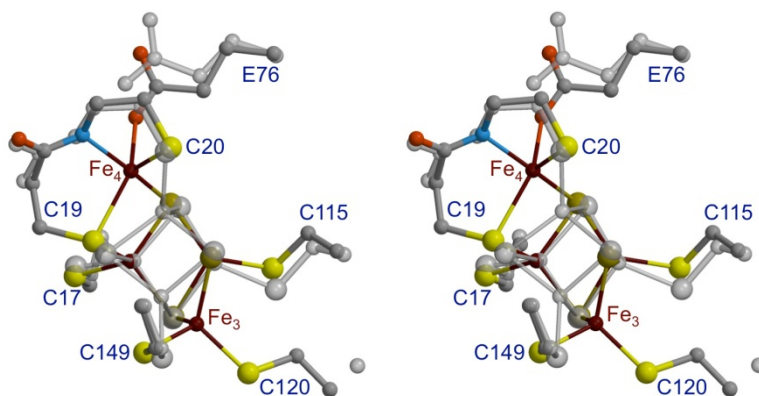


**Figure S2.** Stereo pair of the superposition of the oxidized proximal cluster of *EcHyd-1* (color-coded atoms) onto the proximal cluster from *D. fructosovorans* [NiFe]-hydrogenase (gray).

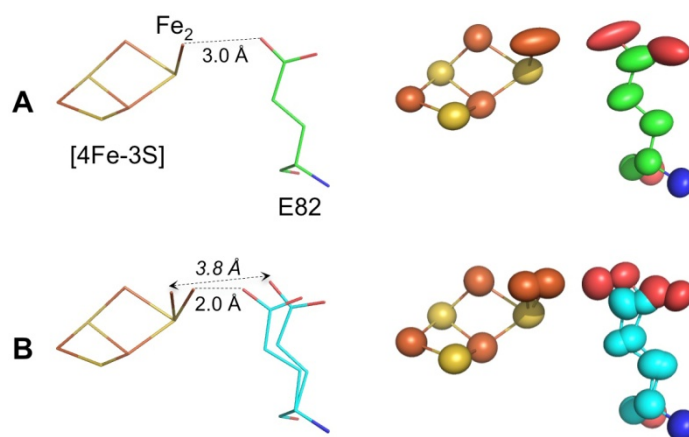


**Figure S3.** Proximal cluster structure of ferricyanide-oxidized *H. marinus* [NiFe]-hydrogenase (33). **A**, as deposited in the PDB (code 3AYY); **B**, after 10 cycles of refinement of the as deposited 3AYY structure with Refmac (11). Two positions were modeled for Glu82 and Fe<sub>2</sub> (Glu76 and Fe<sub>4</sub> in *EcHyd-1*). The unmerged X-ray diffraction intensity data deposited with the 3AYY atomic coordinates were first truncated to Bijvoet-merged structure factor amplitudes, using the programs cif2mtz, combat, sortmtz, scala, truncate and cad of the CCP4 package (13). The R- and R<sub>free</sub>-factor decreased from 12.5 and 15.3 for the starting model to 12.1 and 14.5%, respectively, after refinement. The right side of **A** shows the anisotropy of the deposited atomic temperature factors which is very high for Fe<sub>2</sub> and the side chain atoms of Glu82. When both Fe<sub>2</sub> and Glu82 are refined with two positions the anisotropy virtually disappears (**B**, right). As a consequence, like the oxidized *EcHyd-1* of *E. coli*, about half of the *H. marinus* enzyme may have Glu82 bound to Fe<sub>2</sub>, as suggested by the (closest) Fe-O distance of 2.0 Å after the Refmac refinement (**B**, left). However, two other combinations with Fe<sub>2</sub> and Glu82 separated by about 3 Å cannot be ruled out from X-ray crystallography alone. This figure was prepared with PyMOL (<http://www.pymol.org>).

## 2. Orbital characterization from QM/MM calculations.

Fig. 4, as well as Fig. S4 and Fig. S5, were prepared with the program Maestro (17).

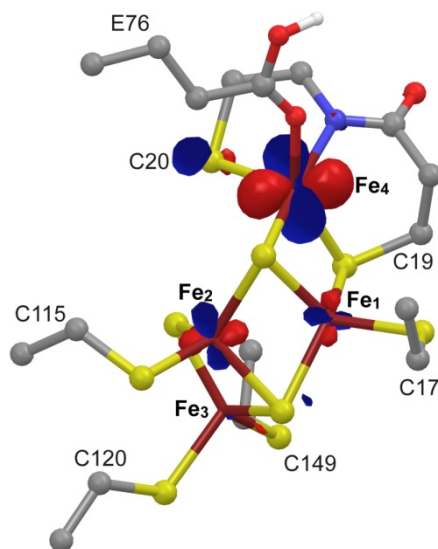


**Figure S4.** Molecular orbital of the PC3<sup>H</sup> model in the BS13 electronic state: LUMO+1,β.

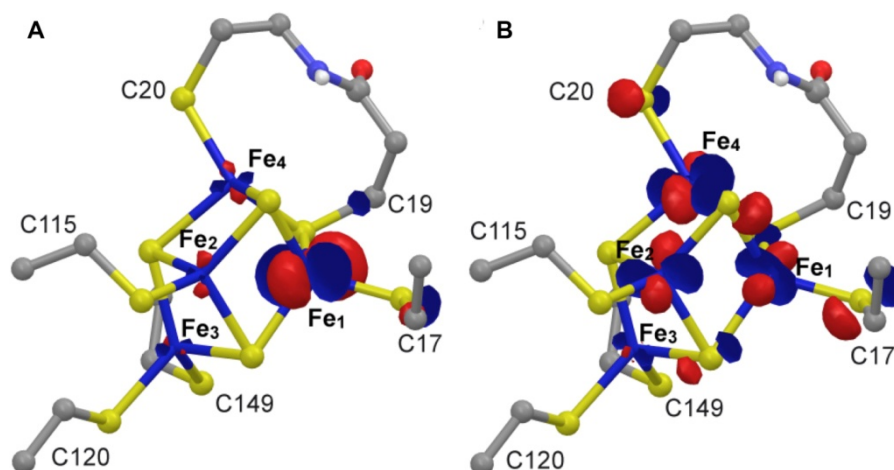


**Figure S5.** Molecular orbitals of the PC2<sup>-</sup> model in the BS13 electronic state: **A**, SOMO  $\alpha$  and **B**, SOMO  $\beta$ .

### 3. Mössbauer parameter calculations.

For all tables, quadrupole splittings  $\Delta E_Q$  are given in mm/s and the asymmetry parameters  $\eta$  are given in parentheses.

Among the small QM models for PC3<sup>H</sup> extracted to calculate the Mössbauer parameters, the BS23 and BS14 electronic states are the least stable, being 50-60 kJ/mol higher than BS13, BS24, BS34 and BS12 (Table S2). This tendency is also verified in models for PC3<sup>-</sup>. Both BS23 and BS14 exhibit enforced ferromagnetically coupled pairs (23 and 14; see Fig. 3) whereas, in the absence of a double exchange mechanism, sulfur (cysteinyl and/or sulfide) bridges normally mediate antiferromagnetism between Fe atoms in [FeS] clusters (34). The cost of such enforcements can be estimated to be of the same order (around 60 kJ/mol: see details in next section). Moreover, their calculated quadrupole splittings  $\{\Delta E_Q\}$  are very different from the experimental ones (24). Both BS23 and BS14 can therefore be definitely ruled out as models for the ground state of PC3 (Table S2). We draw the same conclusions for the corresponding models with deprotonated Glu76 (Table S3).

**Table S2.** PC3<sup>H</sup> model with the customized functional B3LYP (HF=5%).

Electronic State	Relative energies (kJ/mol)	$\Delta E_Q$ Fe <sub>1</sub> ( $\eta$ )	$\Delta E_Q$ Fe <sub>2</sub> ( $\eta$ )	$\Delta E_Q$ Fe <sub>3</sub> ( $\eta$ )	$\Delta E_Q$ Fe <sub>4</sub> ( $\eta$ )
<b>BS13</b>	8.1	2.36 (0.21)	0.31 (0.44)	-0.31 (0.29)	0.96 (0.60)
<b>BS24</b>	<b>0.0</b>	2.14 (0.21)	0.27 (0.45)	-0.35 (0.24)	2.09 (0.77)
<b>BS34</b>	9.9	1.65 (0.93)	0.49 (0.52)	-0.20 (0.46)	2.12 (0.51)
<b>BS23</b>	58.7	0.56 (0.62)	1.11 (0.68)	0.72 (0.40)	1.35 (0.40)
<b>BS12</b>	1.4	1.54 (0.97)	0.44 (0.33)	-0.24 (0.22)	0.80 (0.83)
<b>BS14</b>	60.4	1.23 (0.70)	0.37 (0.97)	-0.45 (0.37)	1.55 (0.28)

Among the four remaining states (Table S2, PC3<sup>H</sup>), BS24 and BS12 can be also ruled out. In the case of BS24, both Fe<sub>1</sub> and Fe<sub>4</sub> exhibit large Mössbauer quadrupole splittings above 2.0 mm/s, contrary to experiment which shows only one large splitting at 2.41 mm/s. Although Fe<sub>4</sub> is ferrous, the quadrupole splitting on Fe<sub>1</sub> (initially constructed as ferric) is surprisingly large, indicating an additional draining of electronic charge from the immediate



surroundings. This underscores the intrinsic tendency of this Fe<sub>1</sub> site to be ferrous (see below). In BS12, Fe<sub>1</sub> is indeed the most reduced ion, although its moderately large  $\Delta E_Q$  value of 1.54 mm/s is too small when compared to experiment: 2.41 mm/s. Again, the same reasoning applies to the corresponding deprotonated Glu76 models (see Table S3).

**Table S3.** PC3<sup>-</sup> model with the customized functional B3LYP (HF=5%).

Electronic State	Relative energies (kJ/mol)	$\Delta E_Q$ Fe <sub>1</sub> ( $\eta$ )	$\Delta E_Q$ Fe <sub>2</sub> ( $\eta$ )	$\Delta E_Q$ Fe <sub>3</sub> ( $\eta$ )	$\Delta E_Q$ Fe <sub>4</sub> ( $\eta$ )
BS13	12.2	2.42 (0.17)	0.43 (0.42)	-0.32 (0.52)	0.79 (0.03)
BS24	27.9	2.38 (0.82)	0.37 (0.38)	-0.26 (0.66)	2.43 (0.98)
BS34	17.3	1.70 (0.57)	0.68 (0.40)	0.27 (0.94)	2.43 (0.90)
BS23	43.9	0.51 (0.28)	1.20 (0.60)	0.85 (0.48)	0.86 (0.82)
BS12	<b>0.0</b>	1.51 (0.85)	0.56 (0.55)	-0.24 (0.97)	0.65 (0.59)
BS14	60.5	2.10 (0.26)	-0.32 (0.81)	0.40 (0.54)	-0.48 (0.87)

Finally, the BS13 and BS34 states with protonated Glu76 exhibit large  $\Delta E_Q$  values of 2.36 and 2.12 mm/s, respectively (Table S2). Concerning their respective intermediate  $\Delta E_Q$  values at 0.96 and 1.65 mm/s, the former is closer to experiment (1.23 mm/s). Moreover, in BS13 Fe<sub>1</sub> is ferrous whereas in BS34 the more reduced site is Fe<sub>4</sub>. Chemical inference would favor the BS13 state with ferric Fe<sub>4</sub>, as it is bound to an anionic amido nitrogen (see Discussion). Finally, our calculations favor a BS13 state in PC3<sup>H</sup> as the predicted  $\Delta E_Q$  value for PC3<sup>-</sup> of 0.79 mm/s is low relative to experiment. The PC3<sub>d</sub><sup>-</sup> state could also correspond to BS13 as its predicted quadrupole splittings are also close to experimental values (Table S4).

**Table S4.** PC3<sub>d</sub><sup>-</sup>-like model where Glu76 has been removed from the PC3<sup>H</sup> model with the customized functional B3LYP (HF=5%).

Electronic State	Relative energies (kJ/mol)	$\Delta E_Q$ Fe <sub>1</sub> ( $\eta$ )	$\Delta E_Q$ Fe <sub>2</sub> ( $\eta$ )	$\Delta E_Q$ Fe <sub>3</sub> ( $\eta$ )	$\Delta E_Q$ Fe <sub>4</sub> ( $\eta$ )
BS13	<b>0.0</b>	2.36 (0.25)	0.27 (0.48)	-0.31 (0.24)	-0.92 (0.95)
BS24	3.7	1.94 (0.27)	0.21 (0.72)	-0.36 (0.24)	2.02 (0.64)
BS34	15.5	1.65 (0.97)	0.47 (0.54)	-0.20 (0.41)	2.00 (0.32)

#### 4. Exchange coupling pathways for the PC3<sup>H</sup> model.

Fig. 3 (main text) depicts the exchange coupling pathways expected for PC3, here illustrated in the case of the BS13 state. As a first rule of thumb, iron atoms embedded with a local pseudo-tetrahedral sulfur environment are expected to be high-spin:  $S(\text{Fe}^{3+}) = 5/2$  and  $S(\text{Fe}^{2+}) = 2$ . This will be obviously the case for iron sites 1-3, and we computationally found it to be always the case for the distorted penta-coordinated Fe<sub>4</sub> environment comprised of two cysteinyl / one sulfide sulfur atoms, as well as one glutamate oxygen and one deprotonated amide nitrogen.

As a second rule of thumb, iron sites bridged by sulfur (cysteinyl / sulfide) atoms will be antiferromagnetically spin-coupled unless double exchange electronic delocalization occurs within the mixed valence pair (see next



section). This will lead to the so-called spin-frustration as the antiferromagnetic spin alignments cannot be satisfied within all six iron-iron pairs. In the case of PC3, spin frustration will occur within both triads (1-2-3) and (1-2-4). The consequences on the spin-coupling schemes will be examined below.

First, let us consider the protonated glutamate case. It can be seen (Table S2) that BS23 and BS14 are the highest in energy (around 60 kJ/mol above the lowest BS states). The reason is clear as both states exhibit enforced ferromagnetic exchange coupling within both the 2-3 and 1-4 iron pairs, which, from charge analysis, are localized. The cost of such enforcement can be estimated. In fact, a rough estimate of  $\langle J \rangle$ , the average exchange coupling constant within the iron-sulfur cluster, can be directly obtained from the energy difference between the HS state on the one hand and the lowest BS state on the other hand as  $E_{\text{HS}} - E_{\text{BS}} = 45 \langle J \rangle$  (34). Numerically, we found  $E_{\text{HS}} - E_{\text{BS}} = 1.36$  eV (protonated glutamate), and therefore  $\langle J \rangle \approx 240$  cm<sup>-1</sup>. Now, the contribution of a given iron pair  $\{i,j\}$  in a BS state to the Heisenberg spin Hamiltonian describing the spin energetics of the cluster is given by  $-J_{ij} M_{Si} M_{Sj}$ . Considering one ferric pair for which  $M_{Si} M_{Sj} = \pm 25/4$ , and one mixed-valence pair for which  $M_{Si} M_{Sj} = \pm 5$ , the cost of flipping one spin within each pair (from the preferential antiferromagnetic coupling to the enforced ferromagnetic coupling) would be on average  $2 \langle J \rangle (25/4 + 5) = (45/2) \langle J \rangle$ . With the previously estimated value of  $\langle J \rangle$ , we find a total energetic cost of 64 kJ/mol, in excellent agreement with the relative energies found for both BS23 and BS14. As a consequence, from energetics alone, we can exclude BS23 and BS14 from representing the ground-state of PC3.

## 5. Spin coupling procedure leading to the g-tensors.

The high potential (HP) cluster PC3 is reported to exhibit an EPR signal with very little anisotropy. In the legend of Figure S8 of Pandelia *et al.* (24), it is also stated that the g-tensor could not be accurately determined. Still, from the simulation of the PC3 center, the three following values have been proposed:  $g_{\text{max}} = 2.015$ ,  $g_{\text{int}} = 2.010$  and  $g_{\text{min}} = 1.990$ , that is  $\Delta g = g_{\text{max}} - g_{\text{min}} = 0.025$  (serving as an index of the anisotropy).

The key point to compute the total g-tensor is to construct a spin-coupling procedure leading to the appropriate spin-coupling coefficients  $\{K_i\}$ . To understand how we designed specific spin-coefficients for PC3, we start by quickly explaining how these are constructed for a standard pseudo-cubane high-potential [4Fe-4S] cluster. In such a cluster, the four iron atoms occupy the summits of a pseudo-tetrahedron, that is, each iron spin interacts with the three other iron spins via predominantly antiferromagnetic super-exchange mechanisms mediated by the sulfide bridges. This also leads to spin frustration. In practice, because of the high symmetry of the cluster, electronic delocalization usually imposes ferromagnetism within the mixed-valence pair via the additional double-exchange mechanism, leading to a local pair spin of 9/2. Each ferric ion ‘sees’ therefore both mixed-valence ions. This alone would lead to a spin  $S = 5$  for the ferric pair. But antiferromagnetism within the ferric pair cants the ferric ions’ spins and lowers that pair spin value from 5 to 4. As a consequence, the resulting cluster spin  $S = 1/2$  is aligned with that of the mixed-valence pair, and the spin-coupling coefficients are positive for the mixed-valence ions ( $K(\text{Fe}^{2.5+}) = +11/6 \approx 1.833$ ) and negative for the ferric ions ( $K(\text{Fe}^{3+}) = -4/3 \approx -1.333$ ). From  $g_{\text{tot}} = \sum_k K_k g(\text{Fe})_k$ , we would have:  $g_{\text{tot}} = 2 \times 1.833 \times g(\text{Fe}^{2.5+}) - 2 \times 1.333 \times g(\text{Fe}^{3+})$ .

The source of the anisotropy being the extra reducing electron embedded within the delocalized mixed-valence pair, and therefore in  $g(\text{Fe}^{2.5+})$ , the large and positive value of  $K(\text{Fe}^{2.5+})$  would amplify the effect of such a local anisotropy. Typically, a HiPIP cluster exhibits the following experimental g-tensor components: 2.12-2.14, 2.04 and 2.03 (i.e. large tensor anisotropy:  $\Delta g \approx 0.10$ ).

First, compared to a standard [4Fe-4S] pseudo-cubane, the iron and sulfur atoms’s arrangement in PC3 is quite different (see Fig. 3), with no obvious symmetry. Consequently, an alternative spin-coupling scheme has to be designed for a very different set of super-exchange pathways.

**BS13.** In the case of BS13, the proposed spin-coupling scheme is constructed as follows. The ferrous ion is located on  $\text{Fe}_1$  ( $S_1 = 2$ ) and the ferric ion on  $\text{Fe}_3$  ( $S_3 = 5/2$ ). Both are antiferromagnetically spin-coupled to the  $\text{Fe}_2$  spin, and are therefore forming a parallel aligned mixed-valence pair of spin 9/2. We therefore first construct the pair spin  $S_{13} = 9/2$  as a localized mixed-valence pair, resulting in:

$$k_3 = (1/2) + [S_3(S_3+1) - S_1(S_1+1)]/[2S_{13}(S_{13}+1)]$$

$$k_1 = (1/2) - [S_3(S_3+1) - S_1(S_1+1)]/[2S_{13}(S_{13}+1)]$$

where, by construction,  $k_1 + k_3 = 1$ . This spin  $S_{13} = 9/2$  is then antiferromagnetically coupled to the  $\text{Fe}_2$  spin  $S_2 = 5/2$  resulting in  $S_{123} = 2$  :

$$k_{13} = (1/2) + [S_{13}(S_{13}+1) - S_2(S_2+1)]/[2S_{123}(S_{123}+1)]$$

$$k_2 = (1/2) - [S_{13}(S_{13}+1) - S_2(S_2+1)]/[2S_{123}(S_{123}+1)]$$

where, again by construction,  $k_{13} + k_2 = 1$ . Finally, the triad spin  $S_{123} = 2$  is antiferromagnetically spin-coupled to the remaining  $S_4 = 5/2$ , resulting into the total cluster spin  $S = 1/2$ :

$$k_{123} = (1/2) + [S_{123}(S_{123}+1) - S_4(S_4+1)]/[2S(S+1)]$$

$$k_4 = (1/2) - [S_{123}(S_{123}+1) - S_4(S_4+1)]/[2S(S+1)]$$

with  $k_{123} + k_4 = 1$ . Rules applying to successive spin-couplings result in:

$$K_1 = k_{123} \times k_{13} \times k_1$$

$$K_2 = k_{123} \times k_2$$

$$K_3 = k_{123} \times k_{13} \times k_3$$

$$K_4 = k_4$$

The corresponding values of the spin coupling coefficients are reported in Table S5.

**BS34.** In the case of BS34, the same reasoning applies as above to BS13. Here, spin frustration occurs within the ferric triad (1,2,3). The ferric ion on  $Fe_3$  is proposed to be antiferromagnetically coupled to both ferric ions on  $Fe_1$  and  $Fe_2$ . The steps leading to the final spin-coupling scheme are as follows:

$$k_1 = (1/2) + [S_1(S_1+1) - S_2(S_2+1)]/[2S_{12}(S_{12}+1)]$$

$$k_2 = (1/2) - [S_1(S_1+1) - S_2(S_2+1)]/[2S_{12}(S_{12}+1)]$$

where, by construction,  $k_1 + k_2 = 1$ . This spin  $S_{12} = 5$  is then antiferromagnetically coupled to both  $Fe_3$  and  $Fe_4$ . Starting for example with  $Fe_4$  of spin  $S_4 = 2$ , this results in  $S_{124} = 3$ :

$$k_{12} = (1/2) + [S_{12}(S_{12}+1) - S_4(S_4+1)]/[2S_{124}(S_{124}+1)]$$

$$k_4 = (1/2) - [S_{12}(S_{12}+1) - S_4(S_4+1)]/[2S_{124}(S_{124}+1)]$$

where, again by construction,  $k_{12} + k_4 = 1$ . Finally, the triad spin  $S_{124} = 3$  is antiferromagnetically spin-coupled to the remaining  $S_3 = 5/2$ , resulting in the total cluster spin  $S = 1/2$ :

$$k_{124} = (1/2) + [S_{124}(S_{124}+1) - S_3(S_3+1)]/[2S(S+1)]$$

$$k_3 = (1/2) - [S_{124}(S_{124}+1) - S_3(S_3+1)]/[2S(S+1)]$$

with  $k_{124} + k_3 = 1$ . Rules applying to successive spin-couplings result in:

$$K_1 = k_{124} \times k_{12} \times k_1$$

$$K_2 = k_{124} \times k_{12} \times k_2$$

$$K_3 = k_3$$

$$K_4 = k_{124} \times k_4$$

The corresponding values of the spin coupling coefficients are reported in Table S5.

**Table S5.** Spin-coupling coefficients for PC3

BS states	$K_1$	$K_2$	$K_3$	$K_4$
<b>BS13</b>	$-88/81 \approx -1.086$	$10/9 \approx 1.111$	$-110/81 \approx -1.358$	$7/3 \approx 2.333$
<b>BS34</b>	2	2	$-5/3 \approx -1.667$	$-4/3 \approx -1.333$

We finally computed the local g-tensors for the three BS states and obtained the total g-tensor predicted for PC3 from  $g_{\text{tot}} = \sum_k K_k g(\text{Fe})_k$ . The resulting DFT-computed g-tensor components (after spin-coupling) in the case of protonated glutamates are given in Table S6. It can be verified that BS13 exhibits, after spin-coupling, the best  $S = 1/2$  total g-tensor. Particularly, the small experimental g-anisotropy is nicely reproduced.

**Table S6.** EPR (g-tensor) calculations for the PC3 state. The three g-tensor eigenvalues  $g_{\max} > g_{\text{int}} > g_{\min}$  were computed for both BS13 and BS34 states except for a constant and unknown  $\Delta g_{\text{iso}}$  shift. The calculated g-tensor anisotropy:  $\Delta g = g_{\max} - g_{\min}$ , is compared to the corresponding experimental value.

	$g_{\max}$	$g_{\text{int}}$	$g_{\min}$	$\Delta g$
<b>BS13 PC3<sup>H</sup></b>	2.043	2.031	2.007	0.036
<b>BS13 PC3<sup>-</sup></b>	2.045	2.021	1.988	0.057
<b>BS13 PC3<sub>d</sub><sup>-</sup></b>	2.057	2.040	2.011	0.046
<b>BS34 PC3<sup>H</sup></b>	2.058	2.046	2.009	0.051
<b>BS34 PC3<sup>-</sup></b>	2.052	2.031	2.002	0.050
<b>BS34 PC3<sub>d</sub><sup>-</sup></b>	2.057	2.038	2.003	0.054
<b>Exp. PC3</b>	2.015	2.010	1.990	0.025

For the sake of comparison, we finally give the values these total g-tensors would have if the standard HiPIP spin-coupling procedure had been used (Table S7).

**Table S7.** The three g-tensor eigenvalues  $g_{\max} > g_{\text{int}} > g_{\min}$  have been computed for both BS13 and BS34 apart from a constant and unknown shift  $\Delta g_{\text{iso}}$  (see Materials & Methods). The spin-coupling procedure and resulting spin-coupling coefficients leading to these values correspond here to the standard HiPIP [4Fe-4S] cluster.

	$g_{\max}$	$g_{\text{int}}$	$g_{\min}$	$\Delta g$
<b>BS13</b>	2.071	2.033	2.019	0.052
<b>BS24</b>	2.079	2.016	1.994	0.085
<b>BS34</b>	2.052	2.016	2.001	0.051
<b>Exp.</b>	<b>2.015</b>	<b>2.010</b>	<b>1.990</b>	<b>0.025</b>

It can be verified now that these last g-tensor anisotropies are larger than those computed for the alternative coupling schemes. Moreover, the components are somewhat closer to those measured for standard HiPIP clusters (notice especially the generally large values of  $g_{\max}$ ).

## 6. Pathways for proton transfer and water escape.

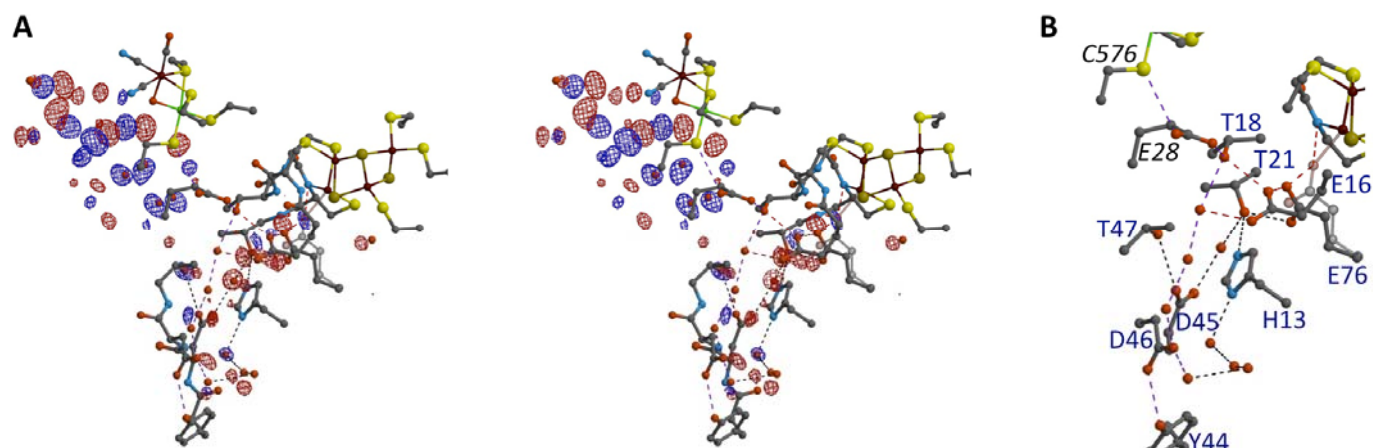


**Figure S6.** **A.** Stereo image of an averaged ( $F_{\text{as isolated}} - F_{\text{H}_2\text{-reduced}}$ ) map superimposed to a partial ball-and-stick representation of the as-isolated *EcHsdR-1* structure, using the color codes of Fig. 5. Positive and negative peaks higher than  $7 \sigma$  are depicted in blue and red, respectively. Dashed lines depict hydrogen bonds. The peaks in the left upper corner suggest a partial water escape pathway, which is highlighted from a different viewpoint in Fig. 5. **B.** Zoom of the lower right corner of **A** showing proposed proton transfer pathways. The hydrogen bonds colored in violet denote a putative pathway from the active site to the molecular surface, whereas those colored in red indicate a connection to the proximal cluster.

## References

1. Dubini A, Pye RL, Jack RL, Palmer T, & Sargent F (2002) How bacteria get energy from hydrogen: a genetic analysis of periplasmic hydrogen oxidation in *Escherichia coli*. *Int. J. Hydrogen Energy* 27:1413-1320.
2. Lukey MJ, *et al.* (2010) How *Escherichia coli* is equipped to oxidize hydrogen under different redox conditions. *J. Biol. Chem.* 285:3928-3938.
3. Vernede X & Fontecilla-Camps JC (1999) A method to stabilize reduced and or gas-treated protein crystals by flash-cooling under a controlled atmosphere. *J. Appl. Crystallogr.* 32:505-509.
4. Kabsch W (2001), eds in International tables for crystallography VF, Crystallography of Biological Macromolecules (Rossmann MG, & and Arnold Ep-, Kluwer Academic Publishers, Dordrecht.).
5. Diederichs K, McSweeney S, & Ravelli RB (2003) Zero-dose extrapolation as part of macromolecular synchrotron data reduction. *Acta Crystallogr.* D59:903-909.
6. Read RJ (2001) Pushing the boundaries of molecular replacement with maximum likelihood. *Acta Crystallogr.* D57:1373-1382.
7. Storoni LC, McCoy AJ, & Read RJ (2004) Likelihood-enhanced fast rotation functions. *Acta Crystallogr.* D60:432-438.
8. McCoy AJ, Grosse-Kunstleve RW, Storoni LC, & Read RJ (2005) Likelihood-enhanced fast rotation functions. *Acta Crystallogr.* D61:458-464.
9. Read RJ (1986) Improved Fourier coefficients for maps using phases from partial structures with errors. *Acta Crystallogr.* A42:140-149.
10. Emsley P, Lohkamp B, Scott WG, & Cowtan K (2010) Features and development of Coot. *Acta Crystallogr.* D66:486-501.
11. Murshudov GN, Vagin AA, & Dodson EJ (1997) Refinement of macromolecular structures by the maximum-likelihood method. *Acta Crystallogr.* D53:240-255.
12. Winn MD, Isupov MN, & Murshudov GN (2001) Use of TLS parameters to model anisotropic displacements in macromolecular refinement. *Acta Crystallogr.* D57:122-133.
13. Anonymous (1994) Collaborative Computational Project Number 4. "The CCP4 Suite: Programs for Protein Crystallography". *Acta Crystallogr.* D50:760-763.
14. Kraulis PJ (1991) Molscript - A program to produce both detailed and schematic plots of structures. *J. Appl. Cryst.* 24:946-950.
15. Merritt EA & Bacon DJ (1997) Raster3D: Photorealistic molecular graphics. *Macromol. Cryst., Pt B, Methods in Enzymology*, Vol 277, pp 505-524.
16. Lawrence MC & Bourke P (2000) CONSCRIPT: a program for generating electron density isosurfaces for presentation in protein crystallography. *J. Appl. Cryst.* 33:990-991.
17. a) Maestro version 9.2 b) QSite version 5.7 c) Jaguar version 7.8 S, LLC, New York, NY, 2011.
18. Volbeda A, *et al.* (2005) Structural differences between the ready and unready oxidized states of [NiFe] hydrogenases. *J. Biol. Inorg. Chem.* 10:239-249.
19. Volbeda A & Fontecilla-Camps JC (2005) Structure-function relationships of nickel-iron sites in hydrogenase and a comparison with the active sites of other nickel-iron enzymes. *Coord.Chem. Rev.* 249:1609-1619.
20. Hay PJ & Wadt WR (1985) Ab initio effective core potentials for molecular calculations - Potentials for K to Au including the outermost core orbitals. *J. Chem. Phys.* 82:299-310.
21. Dunietz BD, *et al.* (2000) Large Scale ab Initio Quantum Chemical Calculation of the Intermediates in the Soluble Methane Monooxygenase Catalytic Cycle. *J. Am. Chem. Soc.* 122:2828-2839.
22. Jorgensen WL, Maxwell DS, & Tirado-Rives J (1996) Development and testing of the OPLS all-atom force field on conformational energetics and properties of organic liquids. *J. Am. Chem. Soc.* 118:11225-11236.
23. Amara P & Field MJ (2003) Evaluation of an ab initio quantum mechanical/molecular mechanical hybrid-potential link-atom method. *Theor. Chem. Acc.* 109:43-52.
24. Pandelia ME, *et al.* (2011) Characterization of a unique [FeS] cluster in the electron transfer chain of the oxygen tolerant [NiFe] hydrogenase from *Aquifex aeolicus*. *Proc. Natl. Acad. Sci. USA* 108:6097-6102.
25. Goris T, *et al.* (2011) A unique iron-sulfur cluster is crucial for oxygen tolerance of a [NiFe]-hydrogenase. *Nature Chem. Biol.* 7:310-318.
26. Szilagyik RK & Winslow MA (2006) On the accuracy of density functional theory for iron-sulfur clusters. *J. Comp. Chem.* 27:1385-1397.
27. Te Velde G & Baerends EJ (1992) Numerical integration for polyatomic systems. *J. Comp. Phys.* 99:84-98.
28. Vosko SH, Wilk L, & Nusair M (1980) Accurate Spin-Dependent Electron Liquid Correlation Energies for Local Spin-Density Calculations - a Critical Analysis. *Can. J. Phys.* 58:1200-1211.
29. Horner O, *et al.* (2007) Spectroscopic description of an unusual protonated ferryl species in the catalase from *Proteus mirabilis* and density functional theory calculations on related models. Consequences for the ferryl protonation state in catalase, peroxidase and chloroperoxidase. *J. Biol. Inorg. Chem.* 12:509-525.
30. Zimmermann R, Ritter G, Spiering H, & Nagy DL (1974) A further example of slow relaxation in high-spin iron(II) compounds: Fe(papt)<sub>2</sub>.C<sub>6</sub>H<sub>6</sub>. *J. Phys.* C6:439-442.

31. Amara P, Mouesca JM, Volbeda A, & Fontecilla-Camps JC (2011) Carbon monoxide dehydrogenase reaction mechanism: A likely case of abnormal CO<sub>2</sub> insertion to a Ni-H<sup>+</sup> bond. *Inorg. Chem.* 50:1868-1878.
32. Orio M & Mouesca JM (2008) Variation of average g values and effective exchange coupling constants among [2Fe-2S] clusters: A density functional theory study of the impact of localization (trapping forces) versus delocalization (double-exchange) as competing factors. *Inorg. Chem.* 47:5394-5416.
33. Shomura Y, Yoon KS, Nishihara H, & Higuchi Y (2011) Structural basis for [4Fe-3S] cluster in the oxygen-tolerant membrane-bound [NiFe]-hydrogenase. *Nature* 479:253-256.
34. Noodleman L, Peng CY, Case DA, & Mouesca JM (1995) Orbital interactions, electron delocalization and spin coupling in iron sulfur clusters. *Coord. Chem. Rev.* 144:199-244.